Gravity wave-induced ionospheric irregularities in the postsunset equatorial valley region

D. L. Hysell[1], D. C. Fritts[2] , B. Laughman[2], and J. L. Chau[3]

[1]Earth and Atmospheric Sciences, Cornell University, Ithaca, New York

[2]GATS Corporation, Boulder, CO

[3]Leibniz Institute für Atmosphären Physik, Kühlingsborn, Germany

Abstract.

Plasma irregularities in the postsunset equatorial valley region ionosphere are investigated experimentally and through numerical simulation. Coherent radar backscatter observed at the Jicamarca Radio Observatory shows two classes of irregularities in different altitude bands – one mainly below about 125 km and the other mainly above. Irregularities in both bands are organized into wavefronts with wavelengths of a few km. However, only the irregularities in the high-altitude band exhibit consistent propagation speeds and directions. Some previous observations of irregularities in the nighttime electrojet suggest that gravity waves may sometimes influence their morphology. The possibility that the valley-region irregularities are also related to gravity waves (GWs) is therefore investigated numerically. A model of a GW packet propagating through a tidal wind field is used to drive another model which predicts the resulting ionospheric electrodynamics. The combined simulation shows that GWs can induce field-aligned currrents and excite resistive drift waves which could be responsible for the valley-region irregularities in the high-altitude band. The GWs also induce irregularities in the upper *E* region directly through simple dynamo action which subsequently deform under the influence of shear flow. This may explain the irregularities in the low-altitude band.

Introduction

The nearly horizontal geomagnetic field lines in the equatorial ionosphere inhibit cross-field plasma transport and dispose it to interchange-type electrostatic plasma instabilities. These include gradient drift instabilities in the *E* region and variants of $\mathbf{E} \times \mathbf{B}$ instabilities in the *F* region. Interchange instabilities occur in regions of inhomogeneous conductivity like the postsunset bottomside *F* region, the bottomside *E* region during the day, and throughout the *E* region at night when the layer is highly structured [*Prakash et al.*, 1972]. Telltales of instability are small-scale plasma density irregularities that cause coherent radar backscatter. Coherent scatter signifies the presence of free energy and offers an incisive way to study the underlying plasma instabilities from the ground. Ionospheric irregularities in the equatorial ionosphere have been reviewed by *Farley* [2009]; *Woodman* [2009]; *Kelley et al.* [2011]; *Hysell et al.* [2014a].

Surprisingly, the equatorial valley region, the "flat" region between the *E*-layer peak and the *F*-region bottomside, is also prone to plasma instability. The region is well known to produce so-called "150-km" echoes during the day (see review by *Chau and Kudeki* [2013] and references therein). Less well known are instabilities responsible for layers of coherent scatter in the valley region at night (e.g. *Patra et al.* [2002]; *Chau and Hysell* [2004]). The echoes and associated irregularities are seen at altitudes as high as about 160 km, well above the electrojet. The layers occur much less frequently than 150-km echoes, electrojet irregularities, and even equatorial spread *F*. They remain sparsely documented and poorly understood.

While the equatorial valley region is often regarded as being nearly homogeneous, structuring in density and composition has been observed in rocket measurements (e.g. *Goldberg et al.* [1974]; *Sinha and Prakash* [1987]; *Goldberg et al.* [1997]; *Raizada and Sinha* [2000]). The structure is often attributed to gravity waves (GWs). GW signatures are clearly evident and

essentially ubiquitous in plasma density profiles in the valley region over Arecibo [*Djuth et al.*, 2010]. At the magnetic equator, incoherent scatter observations also show evidence of internal GWs propagating into the thermosphere [*Varney et al.*, 2009]. GW activity is also prevalent in valley-region HF-reflection profiles observed at Jicamarca. While the source of free energy for 150-km echoes is believed to be photoelectrons [*Oppenheim and Dimant*, 2016], quasi-periodicity in echo morphology at something like the Brunt-Vaisala frequency suggests that GWs may be involved [*Chau and Kudeki*, 2013].

Here, we investigate whether GWs can induce structure and instability in the equatorial post-sunset valley region. Plasma in the upper *E* region is slightly compressible, and winds and wind shears may be able to produce layers where the effects of diffusion and recombination can be overcome. GW wind fields cause bulk motion, with the capacity to push the plasma into an unstable configuration, and current, including field-aligned current, with the capacity to drive instability [*Hysell et al.*, 2002]. At night, photoproduction loses influence, expanding the role of neutral dynamics.

In this paper, we present two sets of observations of valley-region echoes from Jicamarca. We then make comparisons to numerical simulations. Our simulation combines the results from two models — one that predicts the neutral dynamics of GWs in variable backgrounds, and another that predicts the associated plasma dynamics. The comparison helps us understand the response of the equatorial valley region to GWs. It also highlights other plasma processes unique to the region that may be at work.

Observations

Vivid examples of postsunset valley-region echoes were observed at the Jicamarca Radio Observatory on evenings in November, 2003 and September, 2011. The observing mode was

nearly the same in both instances. Transmission was performed using the north and south quarters of the Jicamarca antenna, thereby widening the zonal field of view of the radar. Uncoded pulses were emitted with a 300-m pulse width and an interpulse period (IPP) of 225 km.

Reception was performed using eight receivers, each attached to one of the 64 modules that make up the Jicamarca antenna (plus one outrigger module located to the west of the main array). The particular modules were chosen to represent twenty-eight non-redundant spatial baselines for interferometry including the longest baseline available at Jicamarca which is approximately 100 wavelengths.

Data were processed through the computation of eight spectra and twenty-eight cross spectra for every radar range gate. Data were sorted into 32 Doppler-frequency bins spanning Doppler velocities between $\pm$1000 m/s. Spectral bins outside the range $\pm$250 m/s contained little signal. On the basis of the remaining spectral bins, the signal-to-noise ratio, Doppler shift, and spectral width of the echoes were determined.

Results for Nov. 19, 2003 are shown in Fig. 1. The data are plotted in range-time-Doppler-intensity (RTDI) format. The brightness, hue, and saturation of every pixel in this format represent the signal-to-noise ratio, Doppler shift, and spectral width of the corresponding echo, respectively.

Below about 110-km altitude, the echoes depicted in the figure correspond to irregularities excited by gradient-drift instabilities which are almost always present in the equatorial electrojet. These instabilities are driven by the Cowling current that flows mainly to the east (west) in the electrojet during the day (at night) except during rare counter-electrojet conditions. The coherent backscatter is usually more structured at night when the background density profile becomes more structured [*Farley et al.*, 1994; *Swartz and Farley*, 1994]. Hints of GW features

in nighttime electrojet irregularities have been reported including very large-scale structuring extending over unusually broad altitude spans and spatial timescales [*Swartz and Farley*, 1994; *Patra and Rao*, 1999].

The main features of interest here are the echoes above about 125-km altitude. These echoes were analyzed by *Chau and Hysell* [2004]. They exist in the valley region, above the electrojet but beneath the bottomside of the *F* region in strata where the ions are nearly magnetized. They are generally not as strong as echoes from the electrojet and have smaller Doppler shifts and spectral widths. The echoes shown here have spectra that are slightly blue shifted and very narrow. The echoes seem to be constituted of numerous layers with negative range rates. They persisted for only about 25 min.

Another example of valley echoes is shown in Fig. 2. As in the previous example, these valley echoes manifest as multiple layers with negative range rates. This example differs from the previous one in a number of respects, however. First, the valley echoes persisted for approximately two hours and so were much longer lived. Second, they were confined to a lower range of altitudes between about 110–125. The echoes from the equatorial electrojet were also more structured in this event, particularly toward the end. Additional differences between the two examples are apparent in the radar imagery described below.

Aperture-synthesis radar imaging is used at Jicamarca to reveal the spatial structure of scatterers in the radar-illuminated volume. A detailed discussion of the principles at work and the methods used at Jicamarca is given in *Hysell and Chau* [2006] and references therein. Ours is a super-resolution method with resolution that is not diffraction limited but that depends on the echo signal-to-noise ratio as predicted by the Shannon-Hartley channel-capacity theorem. In practice, the angular resolution of the technique is about 0.1° at Jicamarca. Images are formed

for every Doppler frequency bin separately, and spectral moments are computed and plotted in each pixel of the image. Although images are constructed in three dimensions, two-dimensional cuts are sufficient for rendering the backscatter from field-aligned irregularities. Note that the imagery shown here is more finely resolved in space than that shown by *Chau and Hysell* [2004] which was processed using a different methodology. **The figures are plotted such that the vertical and horizontal spatial dimensions are proportional. Wavelengths can therefore be estimated readily from individual images.**

Selected radar images for the Nov. 19, 2003 event are shown in Fig. 3. The imagery illustrates the evolution of the valley echoes (above about 125 km), echoes from the equatorial electrojet (below about 110 km), and echoes from an intense scattering layer that formed right around 110 km.

The striations in the electrojet region are typical of large-scale waves produced by gradient drift instability in the daytime equatorial electrojet [*Kudeki et al.*, 1982; *Pfaff et al.*, 1987; *Ronchi et al.*, 1991]. These waves have predominate wavelengths of 1-2 km, propagate westward with the convecting electrons under the influence of an upward polarization electric field in the electrojet, and exhibit vertical shear which reflects, in part, altitude variations in the Hall-to-Pedersen conductivity ratio in the *E* region. The morphological characteristics of the large-scale waves in the radar imagery cannot be predicted entirely on the basis of linear plasma theory, particularly during the day, but match predictions of numerical simulations closely [*Ronchi et al.*, 1991; *Hysell and Chau*, 2002].

The strong scattering layer at about 110-km altitude was unusual. Over time, the layer spread in altitude and became inhabited by large-scale waves very similar to the waves in the main part of the electrojet. We may speculate that a sporadic ionization layer created by strong wind shear

formed at about 110 km, extending the region where the electrojet was gradient-drift unstable. We refer to the layer only because it could be interpreted as evidence of strong wind shear.

The most distinctive features in the radar imagery are the bands of scatterers above 125-km altitude. The bands propagated downward and westward with a period of approximately 5 min. **Their wavelength averaged roughly 7–8 km over the event, implying a phase speed of about 25 m/s. Propagation speed and direction were consistent throughout the event.**

Representative radar imagery for the Sep. 5, 2011 event appears in Fig. 4. **It is noteworthy that the large-scale waves in the electrojet itself here had dominant wavelengths of about 5 km which is much larger than the 1–2-km figure from the previous example.** Long wavelengths are typical of large-scale gradient drift waves in the electrojet at night. *Ronchi et al.* [1989] and *Hu and Bhattacharjee* [1999] have interpreted this as a nonlocal effect caused by presumptively jagged nighttime density profiles. Only longer-wavelength waves can grow in this environment, tunneling between altitude strata which are alternatingly stable and unstable to the gradient drift instability. Evidence supporting this theory was presented by *Hysell and Chau* [2002].

Atypically, the waves in the electrojet continued to propagate westward at the lowest altitudes throughout the event shown even though waves in the electrojet normally propagate eastward at night. Eastward propagation is consistent with a downward polarization electric field in the electrojet. The change in direction usually occurs before 20 LT in equinox conditions [*Scherliess and Fejer*, 1999]. Strong winds in the lower thermosphere may therefore have influenced the propagation direction of the waves in this case.

The radar imagery also shows examples of valley echoes between about 110–125 km altitude. As in the previous event, the echoes tended to be organized along wavefronts with wavelengths

of a few km. However, the speed and direction of propagation of the waves was much more variable this time. The waves appear to have been embedded in a region of variable background flow and strong vertical shear that strongly affected their propagation. The apparent motion of the scatterers on the wavefronts was not always normal to the fronts. There were times when the wavefronts were stationary. Wavelengths were not always discernible. In this way, the valley echoes in the Sep. 5, 2011 event were distinctly unlike those in the Nov. 19, 2003 event.

Strong vertical shear characterized the apparent motion of the irregularities at all altitudes in a way that did not simply reflect the Hall-to-Pedersen conductivity ratio profile. For a period after 2100 LT, the apparent flows were rapid and westward, eastward, westward, and eastward at about 98 km, 103 km, 105 km, and above 108 km, respectively. Transitions in the flow direction were abrupt. We attribute the transitions at least in part to neutral dynamics and turn our attention to winds and waves in the neutral lower thermosphere.

Numerical simulations

We describe next a numerical simulation of the neutral and plasma dynamics possibly at work in the equatorial postsunset valley region. Our study considers neutral atmospheric perturbations arising from the interactions of an upward-propagating GW packet with tidal winds in the lower thermosphere as forcing for a separate ionospheric electrodynamics model. The treatment of the neutral dynamics will be described first, followed by the treatment of the plasma dynamics.

Anelastic finite-volume model

The neutral dynamics are described using a finite-volume (FV) code that solves the anelastic Navier-Stokes equations without Coriolis effects. It uses the FV architecture of *Felton and*

Lund [2006] that results in exact numerical conservation of mass, momentum, and kinetic and thermal energy (apart from explicit dissipation) and thus faithfully represents the underlying conservation laws. The FV code has been employed for various studies of mean-flow interactions and instabilities accompanying large-amplitude GWs in two and three spatial dimensions (2D and 3D). These include GW breaking and self-acceleration in simple environments [*Lund and Fritts*, 2012; *Fritts et al.*, 2015], applications to tsunami-driven GW propagation in environments including mean and tidal wind shears, and GW breaking and turbulence transports in mesospheric inversion layers. When achievable 3D resolution is unable to describe turbulence dynamics throughout the inertial range, the FV code uses the dynamic Smagorinsky approach (i.e., *Germano et al.* [1991], modified as suggested by *Lilly* [1996]) to achieve closure.

Our application of the FV code here employs a representative mean temperature profile, $T(z)$, and tidal winds, $U(z)$ in the plane of GW propagation, shown in the upper panels of Fig. 5. The assumed isothermal $T(z)$ = 240 K at lower altitudes yields $N^2 = (g/T)(dT/dz + g/c_p) = 4x10^{-4}$ s^{-2}, where N is the buoyancy frequency, $T_b = 2\pi/N = 314$ s is the buoyancy period, g is the gravitational constant, c_p is the specific heat at constant pressure, and $H = RT/g = 7$ km is density scale height. The tidal fields are those employed in the study by *Laughman et al.* [2017].

Because we sought approximately 2D seed conditions for the electromagnetic code, we performed a 2D FV code simulation describing propagation of a GW packet localized in altitude (and time) into the mesosphere and lower thermosphere (MLT) from below. Initial GW parameters included horizontal and vertical wavelengths, $\lambda_x = \lambda_z = 30$ km (horizontal and vertical wavenumbers $k = 2\pi/\lambda_x$ and $m = 2\pi/\lambda_z$) and an initial intrinsic frequency $\omega_i = k(c - U) = N/1.45$ (with $U = 0$ at lower altitudes and ground-based frequency $\omega = kc$)

related through the appropriate dispersion relation for mid-frequency GWs in the environment specified above (assuming small wind shear and curvature effects):

$$m^2 \;=\; k^2(N^2/\omega_i^2 - 1) - 1/4H^2 \tag{1}$$

The GW was assumed to have a Gaussian packet shape in altitude given by

$$\phi' = \phi'_\circ \exp[-x^2/2\sigma_x^2] \exp[-(z - z_\circ)^2/2\sigma_z^2] \exp[i(k_x x + m_\circ z - \omega t)] \tag{2}$$

with $z_\circ = 20$ km, $\sigma_x = 50$ km, and $\sigma_z = 20$ km, such that it was initially very far from FV code "sponge" layers beginning at 0 and 170 km at the lower and upper FV code boundaries at 50 and 220 km, respectively.

The maximum initial GW horizontal velocity perturbation was $u' = 0.044$ ms^{-1}, and the initial horizontal phase speed was $c = \omega/k = 64.8$ m/s such that $u'/c \ll 1$. The GW was initially linear at lower altitudes but achieved nonlinear amplitudes encountering tidal winds in the MLT. The GW phase speed, c, (dashed line in Fig. 5) was selected to be slightly larger than the eastward tidal wind maximum of 50 ms^{-1} at 100 km so as to promote GW-tidal interactions, including refraction, partial reflection, and instabilities at later times. The resolution was chosen to be 500 m in x and z, leading to a CFL time step for numerical stability of 0.55 s, but a much smaller time step of 0.032 s due to viscous constraints at the highest altitude.

Flow evolution

The flow evolution for this GW-tidal interaction event is shown with $u'(x, z)$ gray-scale cross sections extending from 50–170 km in altitude and 350 km horizontally at 10.5, 21, 31.5, and 42 min after GW packet initiation. The packet propagates upward at the GW vertical group velocity, initially $c_{gz} = 68$ ms^{-1}, prior to encountering the tidal winds. Hence the maximum amplitude reaches ∼63 km at 10.5 min and has encountered the tidal shears prior to 21 min

By 10.5 min., however, the leading edge of the GW packet exhibits significant refraction in the varying tidal winds that increase in altitude. Seen are 1) decreased GW λ_z and ω_i and increased GW shears, du'/dz, in the positive (and increasing) tidal winds at ∼75 and 100 km, 2) the opposite at ∼80-90 km, and 3) apparently vertical phase structures above ∼110 km.

At 21 min, the GW response below ∼80 km has weakened, as this is the trailing edge of the packet, and it now exhibits a superposition of upward- and downward-propagating GWs because of strong reflection above. The GW response near the tidal wind maximum at 100 km has intensified in its amplitude and vertical shear (now a peak amplitude of ∼14 ms^{-1} compared to ∼9 ms^{-1} at 10.5 min and an approximate doubling of du'/dz). The GW amplitude is also larger above ∼110 km, but its phase remains nearly vertical in the central portion of the GW response horizontally because it is evanescent at these altitudes due to a much increased ω_i causing $m^2 < 0$ in Eq. 1 and GW reflection. The increasing GW reflection at this time causes initial horizontal modulation of the strong du'/dz at 100 km. The tendency towards increasing GW amplitudes ($u' \sim 17$ ms^{-1}), vertical shears, and horizontal modulation continues to 31.5 min, and the vertical shears and horizontal modulation increase further by 42 min, but the smaller $\lambda_z \sim 4$ km yield strong GW viscous dissipation thereafter.

Ionospheric electrodynamics model

Wind fields from the neutral dynamics model are used to drive a model of the low-latitude ionosphere. The electrodynamics model code is a more efficient, parallelized version of the one described by *Hysell et al.* [2014b]. It is cast in three dimensions in tilted magnetic dipole coordinates. The simulation solves the continuity and momentum equations for four ion species, O^+, NO^+, O_2^+, and H^+, in a weakly-ionized, quasineutral ionosphere. The species are forced by Coulomb and Lorentz forces, gravity, isotropic pressure, and by the winds. Ion inertia is

neglected. The effects of Coulomb collisions are included in the parallel dynamics only. Chemistry is included but limited to charge-exchange and dissociative recombination reactions. We use a second-order explicit time advance method employing finite-volume monotone upwind schemes for conservation laws (MUSCLs) and total variation limiting flux limiters (see *Trac and Pen* [2003]).

The electrostatic potential is found by enforcing the quasineutrality condition fully in three dimensions. This is a computationally costly calculation but one that allows non-equipotential field lines and electrostatic wave propagation in the direction parallel to the magnetic field. Such waves were found to be potentially important in midlatitude sporadic *E* layers [*Hysell et al.*, 2013]. The computation is carried out using the preconditioned stabilized biconjugate gradient method (PBiCGSTAB) in sparse format. The simulation uses 193, 161, and 145 grid points in the zonal, across-B, and along B directions, giving voxels with a size of roughly 1 km in each dimension. The time step is 2.5 s.

Background thermospheric state parameters are imported from the NRLMSISE-00 model [*Picone et al.*, 2002]. The electron number density is initialized using the PIM model [*Daniell et al.*, 1995], and the initial composition is derived from IRI-2016 [*Bilitza et al.*, 2016]. The background zonal electric field is imported from the *Scherliess and Fejer* [1999] empirical model. Normally, information about the neutral winds is imported from the horizontal wind model (HWM) [*Drob et al.*, 2015]. For these runs, winds are imported from the neutral dynamics model described above. At present, the electrodynamics model supplies no feedback to the neutral dynamics model.

The electrodynamics simulation is initialized for high solar flux, December solstice conditions at Jicamarca at 1815 LT and is matched to the time of GW packet initiation. Whereas the

neutral model is formulated in two dimensions, the ionosphere model is three dimensional. The simulated winds are taken to be uniform in the streamwise direction and periodic in the spanwise direction. They are also taken to be uniform at altitudes above 220 km. The reference frame of the neutral winds is rotated such that the streamwise direction makes a finite (15 deg.) angle with respect to the magnetic meridian plane. This angle is arbitrary and does not strongly affect the simulation results.

The electrodynamics model is capable of simulating gradient drift waves, and large-scale waves emerge in the electrojet early in the simulation. However, these become completely obscured by irregularities forced by the imported GWs. The irregularities and instabilities featured in the discussion that follows are purely consequences of the imposed GW forcing.

Simulation results

The state of the model ionosphere after 10.5 min is shown in Fig. 6. The background density profile reflects a depleted valley region consistent with postsunset recombination. As simulation time elapses, the bottomside *F* region will continue to recombine until little ionization is left in the molecular-dominated strata. Any irregularities forming in the valley region around sunset will be necessarily short lived.

The background flow exhibits rapid westward convection between about 110–200 km altitude and slow eastward convection outside that range, with the strongest shear in the *E* region. The stratified flow is driven by the imposed thermospheric dynamo and shaped by altitude variations in the plasma conductivity in accordance with the quasineutrality condition. While the flows over Jicamarca demonstrate more variability with altitude than we see in Fig. 6, the simulation shows how shears and flow reversals can be forced by winds.

The current density in the equatorial plane is complicated, reflecting the competing influences of Hall, Pedersen, and wind-driven currents in different altitude strata. The currents also have significant vertical components. The current density is mainly westward and downward in the *E* region below about 120 km and eastward and downward above 120 km. The current below 120 km is mainly Hall current below 110 km and direct, wind-driven current above 110 km. Above 120 km, Pedersen current dominates. In the *F* region, the current density rotates from upward to eastward with increasing altitude as is normal for the *F*-region dynamo around sunset [*Haerendel et al.*, 1992]. The currents evolve in local time as the conductivity profiles and background electric field evolve.

Strong field-aligned currents are also present in the model in the *E* region at off-equatorial latitudes. The current is predominantly northward in the simulation, the inter-hemispheric asymmetry being attributable to a combination of solstice conditions and the tilt angle of the neutral forcing. The current extends almost to the equatorial plane on L-shells (constant p surfaces) with apex heights in the valley region. Notice that the bands of current on these L shells bridge different values of p, and the underlying irregularities are not exactly field aligned.

Most importantly, the simulations show the presence of two classes of waves. Below 125 km are *E*-region waves which mirror the structure of the GWs imposed mainly at lower altitudes, somewhere along the magnetic field lines. The waves exhibit very small number density perturbations but more noticeable perturbations in current density. The wavefronts tilt in the direction opposite the shear flow; over time, convection causes them to rotate and realign. The waves are morphologically similar to gradient drift waves but with longer wavelengths. They are forced and not necessarily unstable. Since the GW are transient, the corresponding ionospheric signatures are transient. The GWs could serve as seeds for very long-wavelength gradient drift waves

if the strata involved are gradient-drift unstable. The characteristics of the waves match those of the valley-region echoes observed in the Sep. 5, 2011 event.

At off-equatorial latitudes, field-aligned currents are required to preserve quasineutrality in the vicinity of GW-induced ionospheric irregularities. Without the GWs, the field-aligned currents would be small and regular. With the waves, a pattern of intermittent, choppy field-aligned currents forms.

A separate class of waves predominates in the valley region above about 125-km altitude. These waves inhabit the L-shells where significant field-aligned currents flow. They have significant density perturbations with wavelengths of about 5 km that propagate consistently downward and westward. They are more intense at off-equatorial latitudes than at the magnetic equator and could be regarded as the equatorial signature of primarily off-equatorial plasma waves and instabilities. The waves vanish as the valley region recombines. In terms of where and when they occur, their wavelength, and their direction of propagation, they match the valley-echoes observed in the Nov. 19, 2003 event.

Analysis

The wavelike irregularities in the simulation seen below about 125 km are direct responses to the imposed GWs. At these altitudes, the ions are partially magnetized. Although the GW motion is anelastic, an incompressible neutral flow field will, in general, induce compressible ion motion and generate irregularities locally if the ions are partially magnetized. The process is most effective if the wind field has a curl in the direction of the magnetic field, although this is not a requirement. At lower altitudes, an incompressible neutral flow field cannot induce compressible ion motion since the ions simply follow the neutrals. At higher altitudes where the ions are fully magnetized, only their parallel motion may be compressible. Wind fields

can induce compressible motion and form ionization layers at these altitudes, as in the case of intermediate layers at middle latitudes for example, but again only locally.

However, the irregularities appear above the altitudes where the GW amplitudes are largest. They result from dynamo action. A wind field will generate a dynamo electric field if it has a curl in the direction of the magnetic field, if it has perpendicular divergence in a region of finite Cowling conductivity, or if it has a component parallel to (perpendicular to) a gradient in the Hall (Pedersen) conductivity [*Hysell et al.*, 2002]. These conditions are met in the present case. A dynamo field can subsequently induce compressional motion in partially-magnetized ions and can also induce irregularities in a region of inhomogeneous plasma density through incompressible stirring. In the topside *E* and valley regions, the former mechanism is the more important one.

Dynamo action seems to be ineffective in forming irregularities above about 125 km. The valley-region waves at higher altitudes in the numerical simulation meanwhile have a different nature and seem to be a manifestation of the waves described by *Hysell et al.* [2013] who analyzed so-called "resistive drift waves" in irregular midlatitude sporadic *E*-layer irregularities. Such waves prefer kilometric wavelengths and propagate in a direction intermediate between $\mathbf{E}\times\mathbf{B}$ and $\mathbf{E}\times\mathbf{B}\times\mathbf{B}$. In the present simulations, that means between downward and westward.

The mechanism for resistive drift-wave instability is robust and involves finite field-aligned currents and finite parallel wavenumbers. Under this mechanism, electrons stream parallel to the magnetic field to neutralize potential fluctuations. If the parallel conductivity varies along the field line, the electrons overshoot in such a way that the potential fluctuations grow, leading to instability. The predominant wavelength is related to the parallel conductivity parallel gradient length scale. The requirement that the parallel conductivity vary along B is met most

readily away from the magnetic equator. At middle latitudes, field-aligned currents arise near the boundaries of patchy sporadic *E* layers in order to preserve quasineutrality. Field-aligned currents also arise from GW-induced irregularities in the *E* region at slightly off-equatorial latitudes at the electrojet boundary.

Hysell et al. **[2013] derived a linear, local dispersion relation for the instability and applied it to the analysis of kilometer-scale irregularities in patchy midlatitude sporadic-*E* layers. Such irregularities are relatively compact spatially, making the dispersion relation applicable. The dispersion relation cannot be applied reliably in this case since the valley-region irregularities span a broad range of altitudes and background parameters. It cannot be used therefore to predict precisely the growth rate and dominant wavelength of the valley-region irregularities. However, we can verify the role of resistive drift waves by testing for a crucial characteristic. resistive drift-wave mode, the density and potential fluctuations need to be precisely 135° (2.36 rad.) out of phase.**

Fig. 7 shows the time history of a single Fourier mode in the simulation taken from a neighborhood in wavevector space where power is concentrated. The mode in question has a transverse wavelength of about 5 km, a small but finite parallel wavenumber component, and a downward and westward propagation direction. The figure shows the amplitude and phase of the electron density and the difference in phase between the electron density and the potential. Rapid growth of the wave amplitude proceeds after the phase difference approaches the optimal value and continues until saturation occurs about 6 min into the simulation. This behavior is characteristic of resistive drift waves.

Summary

Valley-region irregularities are enigmatic because they can form at altitudes where the ions are nearly magnetized and the background plasma density profile is relatively flat, seemingly ruling out the possibility that plasma interchange instabilities are responsible. The wavelike nature of the irregularities hints at GWs, and we have therefore investigated the influence of a GW packet in the postsunset equatorial valley region ionosphere. Strong shear flow seems to be ubiquitous in the equatorial MLT region, and so the GW model included a background tidal wind pattern. This severely restricted the GW amplitude above about 110-km altitude. Consequently, the GW packet could not generate plasma irregularities in the upper *E* and valley regions locally.

One possibility for nonlocal irregularity generation is via dynamo action. A GW packet can generate a dynamo electric field through a number of mechanisms that are viable in the equatorial electrojet. The dynamo electric field can produce irregularities by inducing compressible ion motion at altitudes where the ions are partially magnetized. This process seems to be responsible for generating plasma irregularities up through about 125-km altitude in simulation. The irregularities in question would be morphologically similar to large-scale gradient drift waves except with longer wavelengths and broader altitude spans. The modeled GW packet was transient, and so were the irregularities it induced. The overall effect was reminiscent of the valley echoes observed in the Sep. 5, 2011 event over Jicamarca. A similar scenario may have been responsible for the features observed in the nighttime electrojet by *Swartz and Farley* [1994] and *Patra and Rao* [1999].

Another possibility for nonlocal irregularity generation is the resistive drift-wave mechanism. Irregularities produced by GWs directly in the electrojet require field-aligned current to maintain

quasineutrality. These currents can excite drift-wave instabilities where the parallel conductivity varies along the magnetic field line. The waves are imperfectly field aligned. Although the instability operates mainly off the magnetic equator, the signature at the equator is still significant. This mechanism is more consistent with the valley echoes in the Nov. 19, 2003 event.

Valley-region echoes are uncommon in the Peruvian sector, and the examples in this paper are among the most vivid in the Jicamarca database. The mechanisms described in this paper require a strong GW packet to reach the ionosphere precisely at twilight when photoproduction is ceasing but while there is still a valley region to deform. **Gravity waves propagating through tidal layers and driving ionospheric currents is thought to be a common phenomenon, and the reason why valley echoes are relatively uncommon is therefore not obvious. Examining the occurrence statistics of the phenomena in different seasons, parts of the solar cycle, and at different latitudes and longitudes should help resolve the problem.**

Acknowledgments. This research was supported through NASA contract NNX14AN51G and ONR contract N0014-13-01-0488. We also acknowledge the DoD High Performance Computing Modernization Program for valuable access to several supercomputer platforms that allowed the simulations here. The Jicamarca Radio Observatory is a facility of the Instituto Geofisíco del Perú operated with support from NSF award AGS-1433968 through Cornell. The help of the staff is much appreciated. The participation of JLC in this work is part of the project supported by the Deutsche Forschungsgemeinschaft (DFG, German Research Foundation) under SPP 1788 (DynamicEarth) – CH 1482/1-1 (DYNAMITE). Data used for this publication are available through the Madrigal database at http://madrigal.haystack.mit.edu/madrigal/.

References

Bilitza, D., D. Altadill, B. Reinisch, I. Galkin, V. Shubin, and V. Truhlik, The International Reference Ionosphere: Model Update 2016, in *EGU General Assembly Conference Abstracts*, vol. 18, p. 9671, 2016.

Chau, J. L., and D. L. Hysell, High altitude large-scale plasma waves in the equatorial electrojet at twilight, *Ann. Geophys.*, *22*, 4071, 2004.

Chau, J. L., and E. Kudeki, Discovery of two distinct types of equatorial 150-km radar echoes, *Geophys. Res. Lett.*, p. doi/10.1002/grl.50893, 2013.

Daniell, R. E., L. D. Brown, D. N. Anderson, M. W. Fox, P. H. Doherty, D. T. Decker, J. J. Sojka, and R. W. Schunk, PIM: a global parameterization based on first principles models, *Radio Sci.*, *30*, 1499, 1995.

Djuth, F. T., L. D. Z. , D. J. Livneh, I. Seker, S. M. Smith, M. P. Sulzer, J. D. Mathews, and R. L. Walterscheid, Arecibo's thermospheric gravity waves and the case for an ocean source, *J. Geophys. Res.*, *115*, doi:10.1029/2009JA014,799, 2010.

Drob, D. P., et al., An update to the Horizontal Wind Model (HWM): The quiet time thermosphere, *Earth and Space Science*, *2*, doi:10.1002/2014EA000,089, 2015.

Farley, D. T., The equatorial *E*-region and its plasma instabilities: A tutorial, *Ann. Geophys.*, *27*, 1509–1520, 2009.

Farley, D. T., W. E. Swartz, D. L. Hysell, and C. Ronchi, High-resolution radar observations of daytime kilometer-scale wave structure in the equatorial electrojet, *J. Geophys. Res.*, *99*, 299, 1994.

Felton, F. N., and T. S. Lund, Kinetic energy conservation issues associated with the collocated mesh scheme for incompressible flow, *J. Comput. Phys.*, *215*, 465–484, 2006.

Fritts, D. C., B. Laughman, T. S. Lund, and J. B. Snively, Self-acceleration and instability of gravity wave packets: 1. Effects of temporal localization, *J. Geophys. Res. Atmos.*, *120*, 8783–8803, doi:10.1002/2015JD023,363, 2015.

Germano, M., U. Piomelli, P. Moin, and W. H. Cabot, A dynamic subgrid-scale eddy viscosity model, *Phys. Fluids A*, *3*, 1760–1765, 1991.

Goldberg, R. A., A. C. Aikin, and B. B. K. Murthy, Ion composition and drift observations in the nighttime equatorial ionosphere, *Tech. Rep. NASA-TM-X-70593*, NASA Goddard Space Flight Center, 1974.

Goldberg, R. A., G. A. Lehmacher, F. J. Schmidlin, D. C. Fritts, J. D. Mitchell, C. L. Croskey, M. Fredrich, and W. E. Swartz, Equatorial dynamics observed by rocket, radar, and satellite during the CADRE/MALTED campaign: 1. Programmatics and small-scale fluctuations, *J. Geophys. Res.*, *102*, 26,179–26,190, 1997.

Haerendel, G., J. V. Eccles, and S. Cakir, Theory for modeling the equatorial evening ionosphere and the origin of the shear in the horizontal plasma flow, *J. Geophys. Res.*, *97*, 1209, 1992.

Hu, S., and A. Bhattacharjee, Gradient drift instabilities and turbulence in the nighttime equatorial electrojet, *J. Geophys. Res.*, *104*, 28,123–18,132, 1999.

Hysell, D. L., and J. L. Chau, Imaging radar observations and nonlocal theory of large-scale waves in the equatorial electrojet, *Ann. Geophys.*, *20*, 1167, 2002.

Hysell, D. L., and J. L. Chau, Optimal aperture synthesis radar imaging, *Radio Sci.*, *41*, 10.1029/2005RS003,383, RS2003, 2006.

Hysell, D. L., J. L. Chau, and C. G. Fesen, Effects of large horizonbtal winds on the equatorial electrojet, *J. Geophys. Res.*, *107*, doi:10.1029/2001JA000,217, 2002.

Hysell, D. L., E. Nossa, H. C. Aveiro, M. F. Larsen, J. Munro, M. P. Sulzer, and S. A. González, Fine structure in midlatitude sporadic *E* layers, *J. Atmos. Sol. Terr. Phys.*, *103*, 16–23, DOI: 10.1016/j.jastp.2012.12.005, 2013.

Hysell, D. L., R. Jafari, D. C. Fritts, and B. Laughman, Gravity wave effects on postsunset equatorial f region stability, *J. Geophys. Res.*, *119*, 5847–5860, doi:10.1002/2014JA019,990, 2014a.

Hysell, D. L., R. Jafari, M. A. Milla, and J. W. Meriwether, Data-driven numerical simulations of equatorial spread *F* in the Peruvian sector, *J. Geophys. Res.*, p. doi:10.1002/2014JA019889, 2014b.

Kelley, M. C., J. J. Makela, O. de la Beaujardiere, and J. Retterer, Convective ionospheric storms: A review, *Rev. Geophys.*, *49*, doi:10.1029/2010RG000,340, 2011.

Kudeki, E., D. T. Farley, and B. G. Fejer, Long wavelength irregularities in the equatorial electrojet, *Geophys. Res. Lett.*, *9*, 684, 1982.

Laughman, B., D. C. Fritts, and T. S. Lund, Tsunami-driven gravity waves in the presence of vertically varying background and tidal wind structures, *J. Geophys. Res.*, 2017, in press.

Lilly, D. K., A proposed modification of the germano subgridscale closure method, *Phys. Fluids*, *4*, 633–635, 1996.

Lund, T., and D. C. Fritts, Gravity wave breaking and turbulence generation in the thermosphere, *J. Geophys. Res.*, *117*, doi:10.1029/JD017,536, 2012.

Oppenheim, M. M., and Y. S. Dimant, Photoelectron-induced waves: A likely source of 150 km radar echoes and enhanced electron modes, *Geophys. Res. Lett.*, *43*, 3637–3644, doi:10.1002/2016GL068,179, 2016.

Patra, A. K., and P. B. Rao, High-resolution radar measurements of turbulent structure in the low-latitude *E* region, *J. Geophys. Res.*, *104*, 24,667–24,673, 1999.

Patra, A. K., P. B. Rao, V. K. Anandan, A. R. Jain, and G. Viswanathan, Evidence of intermediate layer characteristics in the Gadanki radar observations of the upper E region field-aligned irregularities, *Geophys. Res. Lett.*, *29*, 10.1029/2001GL013,773, 2002.

Pfaff, R. F., M. C. Kelley, E. Kudeki, B. G. Fejer, and K. D. Baker, Electric field and plasma density measurements in the strongly driven daytime equatorial electrojet, 1, The unstable layer and gradient drift waves, *J. Geophys. Res.*, *92*, 13,578, 1987.

Picone, J. M., A. E. Hedin, D. P. Drob, and A. C. Aikin, NRLMSISE-00 empirical model of the atmosphere: Statistical comparisons and scientific issues, *J. Geophys. Res.*, *107, A12*, doi: 10.1029/2002JA009,430, 2002.

Prakash, S., B. H. Subbaraya, and S. P. Gupta, Rocket measurements of ionization irregularities in the equatorial ionosphere at Thumba and identification of plasma irregularities, *Indian J. Radio Space Phys.*, *72*, 1, 1972.

Raizada, S., and H. S. S. Sinha, Some new features of electron density irregularities over SHAR during strong spread F, *Ann. Geophys.*, *18*, 141–151, 2000.

Ronchi, C., P. L. Similon, and R. N. Sudan, A nonlocal linear theory of the gradient drift instability in the equatorial electrojet, *J. Geophys. Res.*, *94*, 1317, 1989.

Ronchi, C., R. N. Sudan, and D. T. Farley, Numerical simulations of large-scale plasma turbulence in the daytime equatorial electrojet, *J. Geophys. Res.*, *96*, 21,263, 1991.

Scherliess, L., and B. G. Fejer, Radar and satellite global equatorial *F* region vertical drift model, *J. Geophys. Res.*, *105*, 6829–6842, 1999.

Sinha, H. S. S., and S. Prakash, Rocket observations of E-region ionization irregularities produced through cross field instability mechanism — Current status, *Ind. J. Radio & Spa. Phys.*, *16*, 102–113, 1987.

Swartz, W. E., and D. T. Farley, High-resolution radar measurements of turbulent structure in the equatorial electrojet, *J. Geophys. Res.*, *99*, 309, 1994.

Trac, H., and U. L. Pen, A primer on Eulerian computational fluid dynamics for astrophysicists, *Astrophysics*, *115*, 303–321, 2003.

Varney, R. H., M. C. Kelley, and E. Kudeki, Observations of electric fields associated with internal gravity waves, *J. Geophys. Res.*, *114, A02304*, doi:10.1029/2008JA013,733, 2009.

Woodman, R. F., Spread F- An old equatorial aeronomy problem finally resolved?, *Ann. Geophys.*, *27*, 1915–1934, 2009.

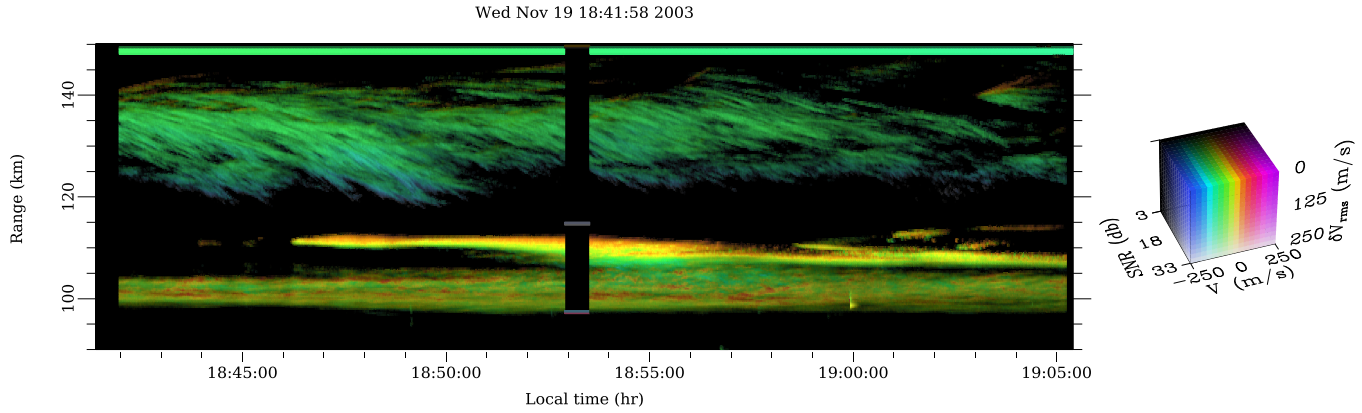

Figure 1. Jicamarca range-time-Doppler-intensity (RTDI) plot of valley-region coherent scatter from Nov. 19, 2003. The legend shows how to interpret the pixels in the figure.

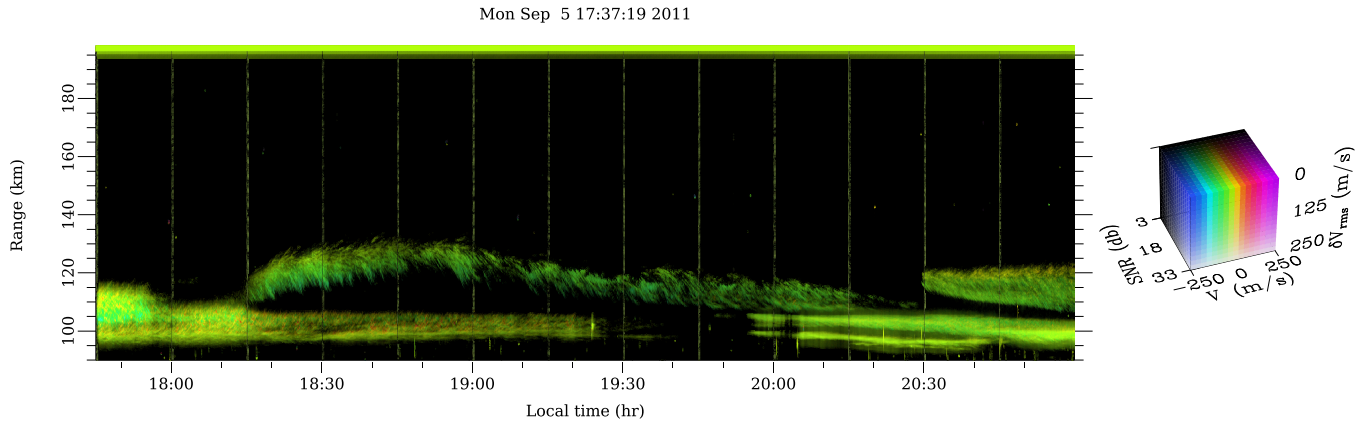

Figure 2. Jicamarca RTDI plot of valley-region coherent scatter from Sep. 5, 2011.

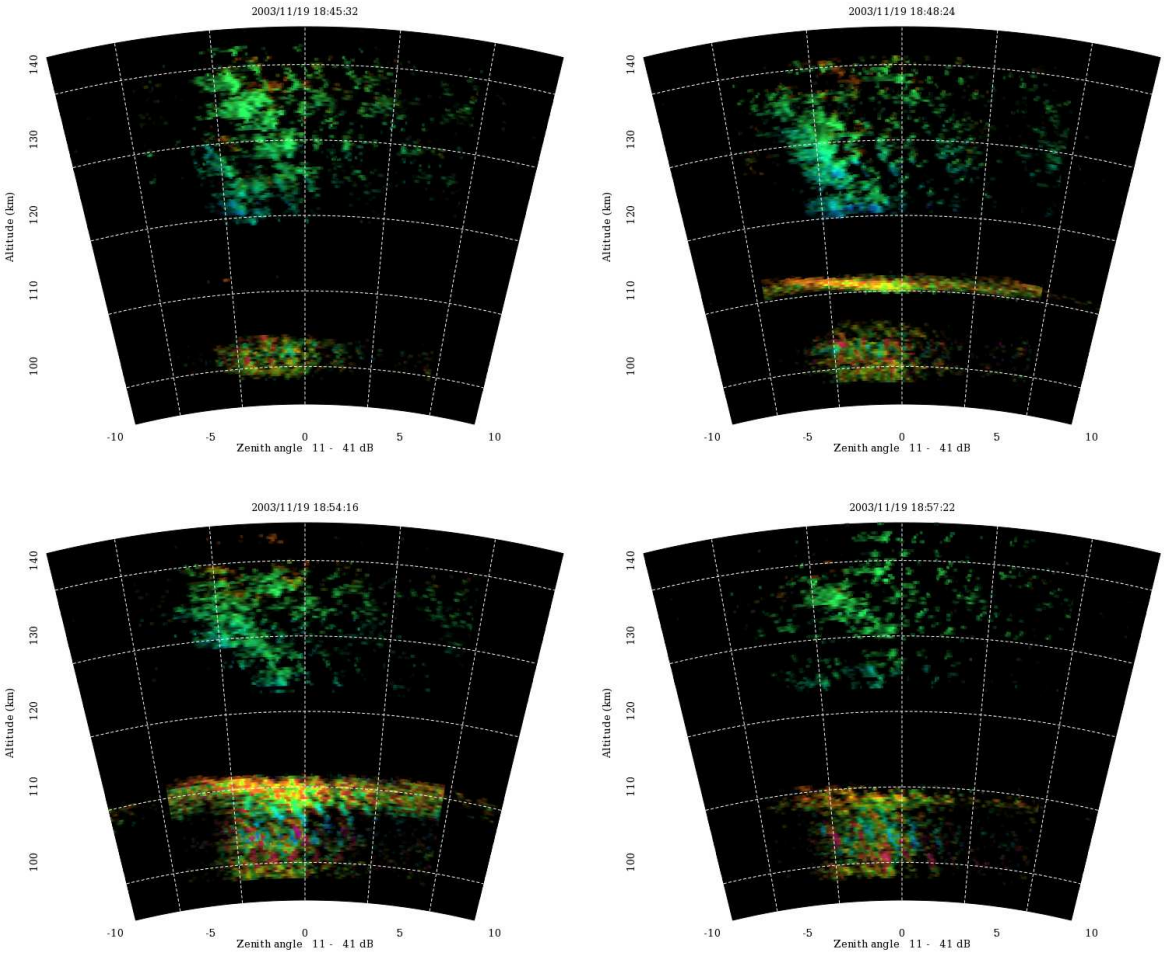

Figure 3. Radar imagery from Nov. 19, 2003 at four different local times. The color scale for the image pixels is the same as for Figures 1 and 2. Note that the Jicamarca transmitter illuminates only the center portion of the field of view.

t

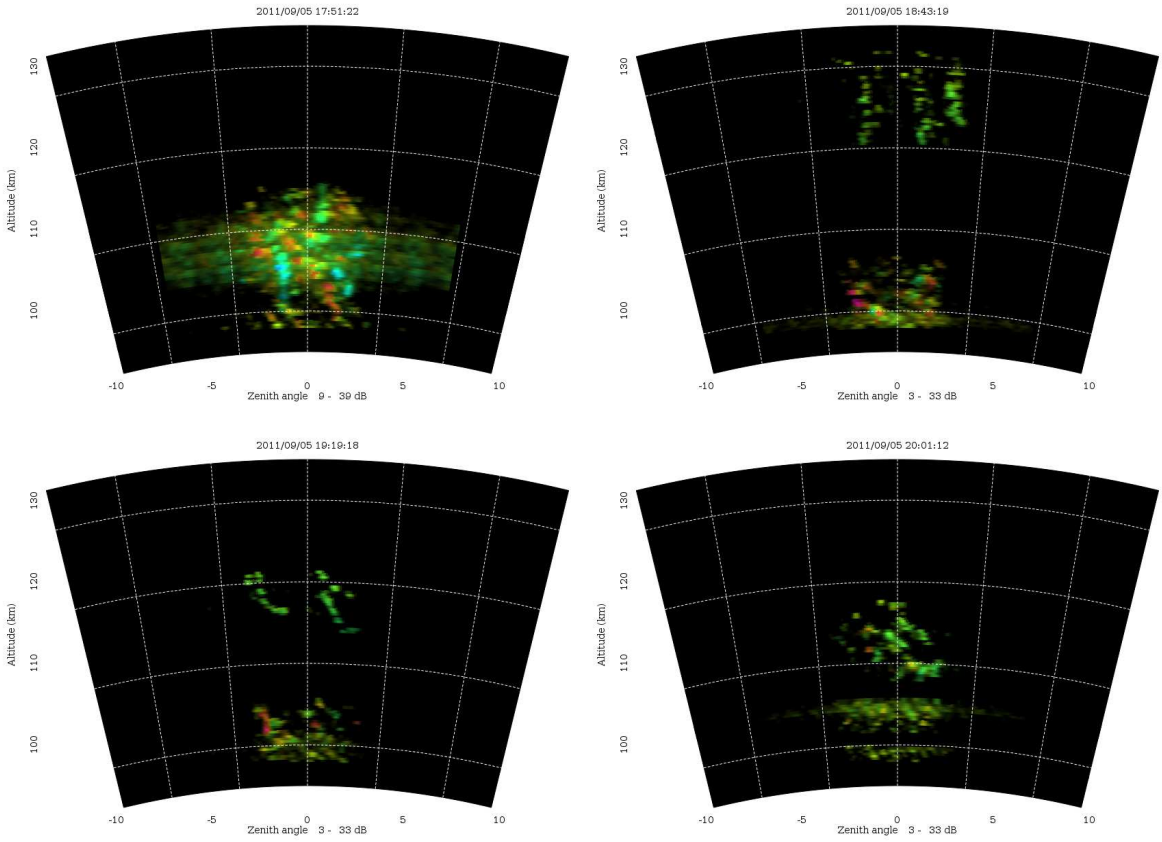

Figure 4. Radar imagery from Sep. 5, 2011.

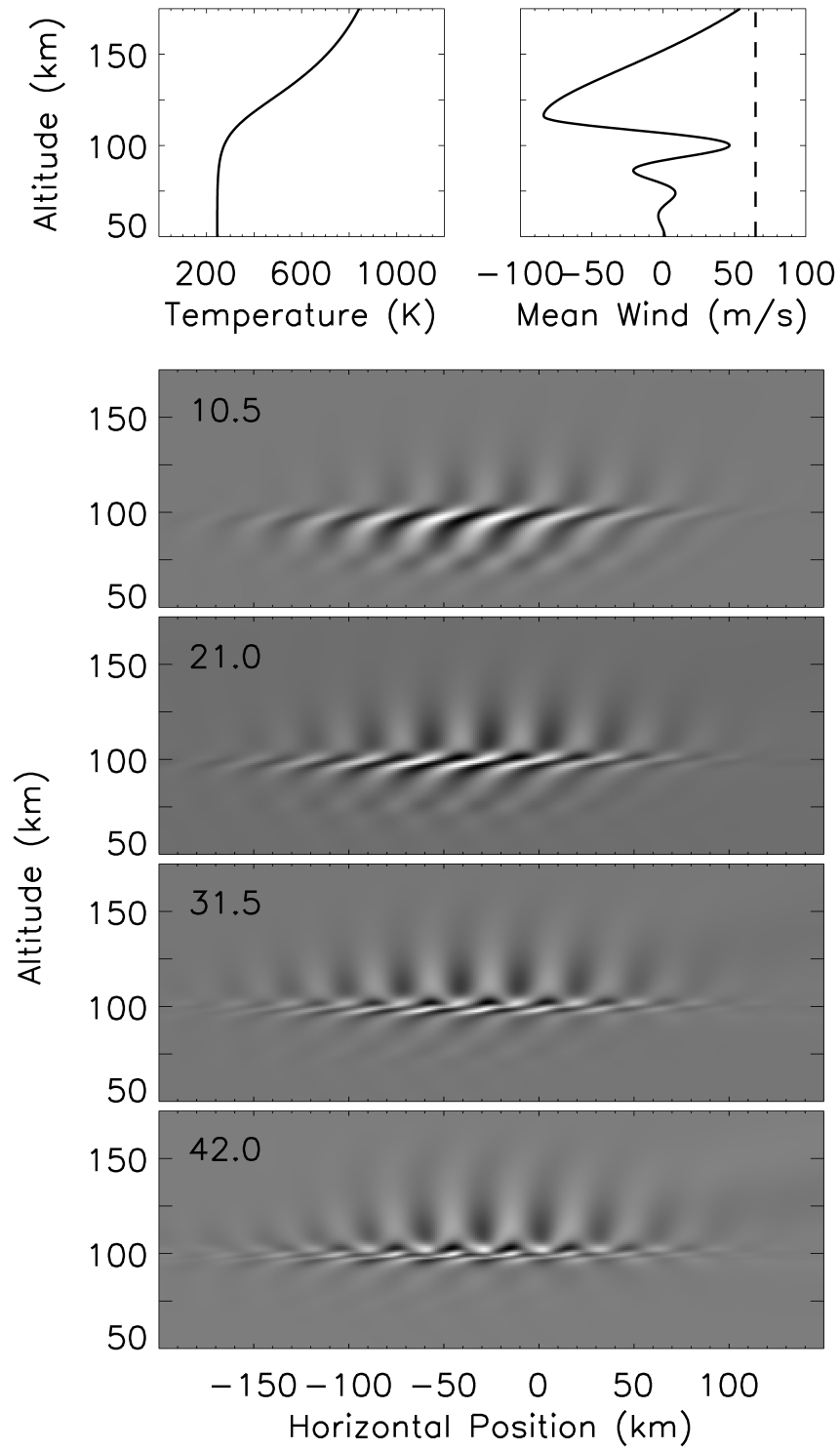

Figure 5. Results from the anelastic finite-volume neutral dynamics model. Top row: background temperature and mean-wind profiles. Remaining rows: Zonal neutral winds in two dimensions at four different times in min. (see text).

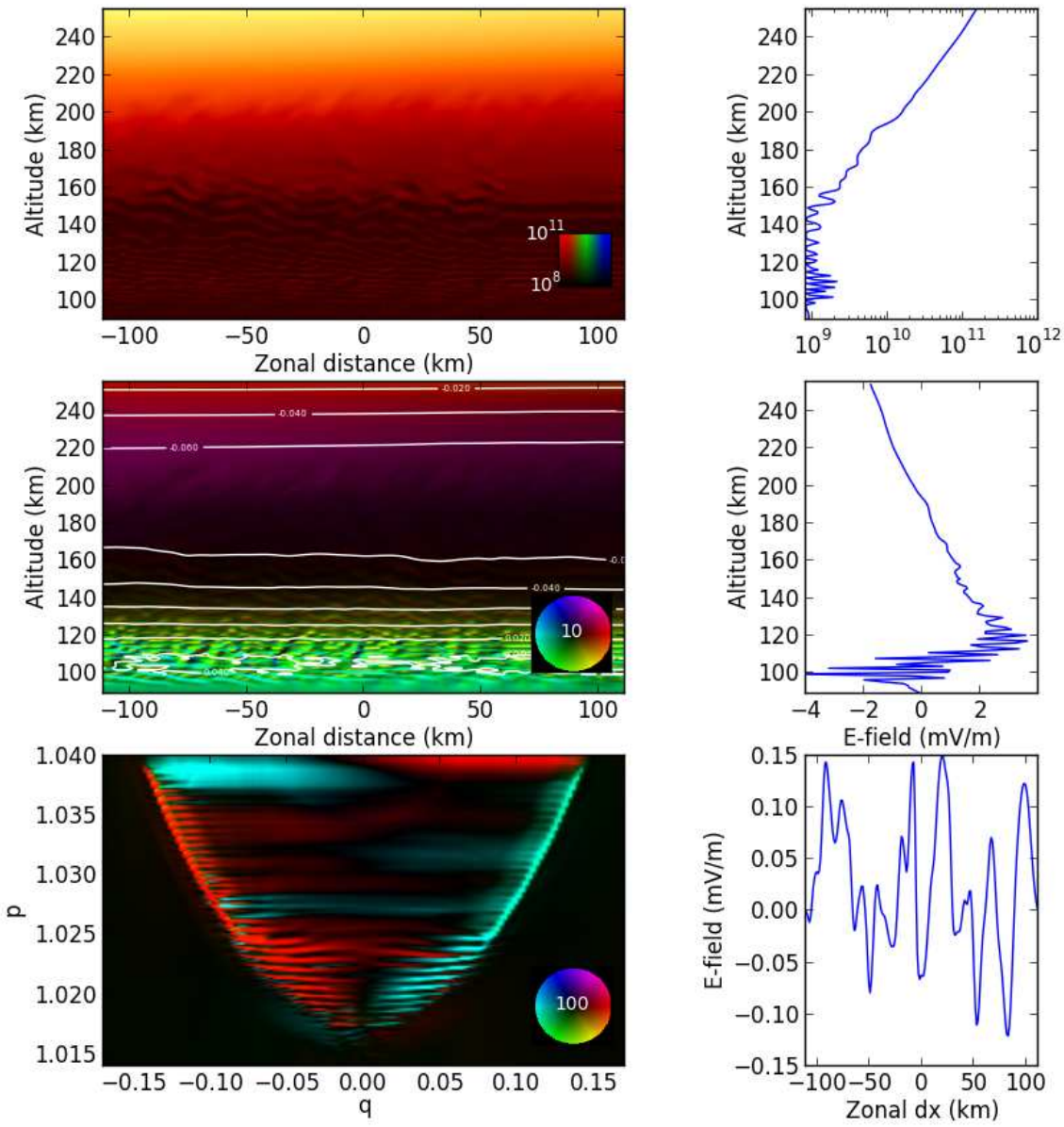

Figure 6. Numerical simulation of valley-region layers 10.5 min. after GW packet initiation. Top row: plasma density and composition. Red, green, and blue hues denote molecular ions, atomic ions, and protons, respectively. To the right is an electron density profile. Middle row: plasma current density. White contours are equipotentials. To the right is a vertical electric field profile. Bottom row: current density in magnetic coordinates (p, q) in the meridional plane. To the right is the zonal electric field. All panels reflect cuts passing through the center of the simulation volume.

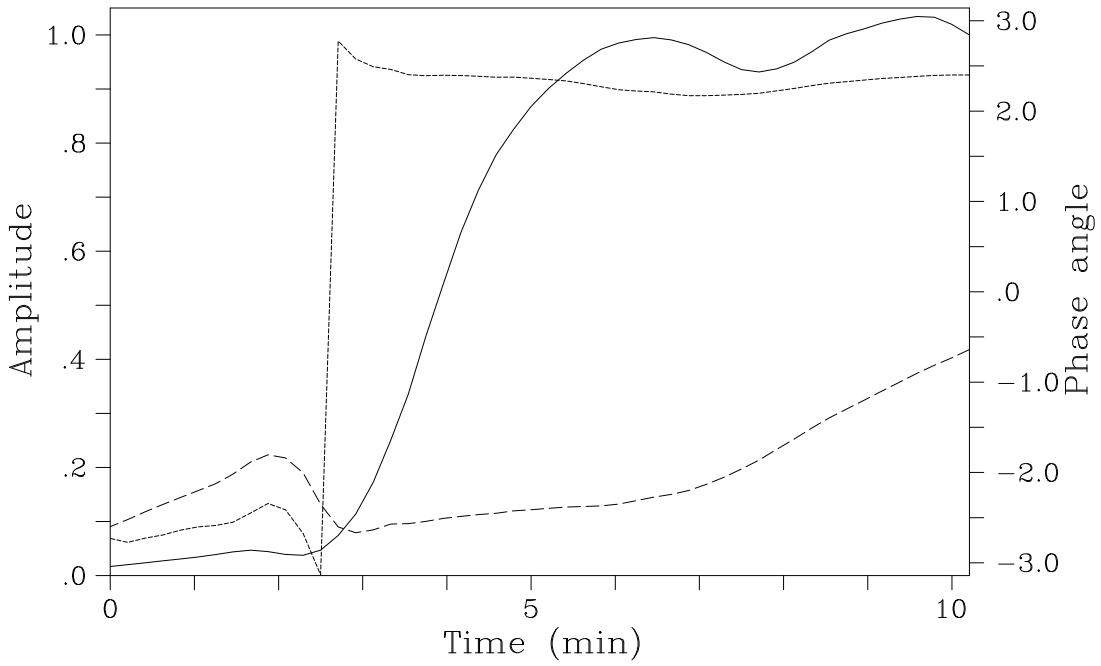

Figure 7. Time history of wave mode representative of valley-region irregularities above 125 km. The solid curve shows the relative amplitude of the mode, and the dashed curve shows the phase. The short dashed curve shows the phase angle difference between the density and the potential. Rapid wave growth occurs after the difference assumes a value close to 135° (2.36 rad). The wave amplitude saturates after about 6 min.